Analysis of Drag Sources in a Fully Submerged Waterjet

MARINE 2021

Filippo Avanzi[1,*], Francesco De Vanna[1], Ernesto Benini[1], Fabio Ruaro[2] and William Gobbo[2]

[1] Department of Industrial Engineering (DII)
Università degli Studi di Padova
via Venezia 1, 35131 Padova (PD), Italy
Web page: https://www.dii.unipd.it/en/

[2] SEALENCE S.p.A.
vicolo San Giorgio 25/27, 20090 Buccinasco (MI), Italy
Web page: https://www.sealence.it

[*] Corresponding author: Filippo Avanzi, filippo.avanzi@phd.unipd.it

ABSTRACT

A parametric study is conducted to optimise the drag performance of a novel concept of ram inlet waterjet. The latter being an outboard device housing the whole propulsion system. The study follows the guidelines from aero-engines literature which account for the pre-entry streamtube drag in the computation of external hydrodynamic resistance. Flow field data are obtained by solving Reynolds-Averaged Navier-Stokes equations, with $k-\omega$ SST turbulence model, on a 2D axisymmetric domain. Reynolds number, based on propulsor's highlight diameter and free stream velocity, is varied between $1.6 \cdot 10^6$ and $2.7 \cdot 10^6$. For each far-field condition, 9 different mass flow rate values are imposed on the internal boundaries corresponding to the pump sections and resulting in an overall range of the machine flow coefficient of 0.32. Comparing performance among three geometries shows that walls' negative gradients drastically affect the drag coefficient in the whole operating envelope. In particular, reduced cross-sectional dimensions and longer shapes favour smoother external outlines. These prove to reduce the system's resistance, despite the augmented axial length. Contextually, the analysis of the capture streamtube through the mass flow capture ratio shows that this parameter is less effective in enhancing performance, especially when the internal geometry is kept unchanged.

Keywords: Podded Waterjet, Nacelle Optimisation, Ram Intake, Electric Propulsion, Outboard Device.

NOMENCLATURE

A_{hl}	Highlight cross-sectional area [m^2]
c_d	Drag coefficient [-]
D_{ave}	Average diameter of the pump section [m]
D_{hl}	Highlight diameter [m]
D_{nac}	Nacelle's drag force [N]
k	Turbulence kinetic energy [m^2 s^{-2}]
$\dot{m}$	Mass flow rate [kg s^{-1}]
p_0	Total pressure [Pa]
$p_{0,\infty}$	Free stream total pressure [Pa]
r_∞	Radius of the far-upstream cross-sectional area [m]
r_{SP}	Radial location of the Stagnation Point [m]
Re	Reynolds number [-]
u	Velocity magnitude [m s^{-1}]
u_∞	Free stream velocity [m s^{-1}]
u_τ	Friction velocity [m s^{-1}]

y_1	Wall distance of the first cell [m]
y_w^+	Wall non-dimensional distance [-]
μ	Dynamic viscosity [Pa s]
μ_w	Dynamic viscosity at the wall [Pa s]
ρ	Fluid density [kg m^{-3}]
ρ_w	Fluid density at the wall [kg m^{-3}]
φ	Machine flow coefficient [-]
ϕ_{nac}	External cowl's drag force [N]
ϕ_{pre}	Pre-entry streamtube's drag force [N]
Ω	Pump angular velocity [rad s^{-1}]
ω	Turbulence specific rate of dissipation [Hz]
MFCR	Mass Flow Capture Ratio
RANS	Reynolds-Averaged Navier-Stokes
SST	Shear Stress Transport

1 INTRODUCTION

Waterjet propulsion systems are of fundamental importance in marine transportation. Travel speeds above 35 knots are generally reached using such systems thanks to higher efficiency than standard screw propellers. Jet propulsors generate thrust as a reaction to the change in the flow momentum between the inlet of an intake and the outlet of an exhaust nozzle (Oh *et al.,* 2003). A bladed pump rotor is used to pressurise the flow within the propulsor assembly and achieve momentum change. A proper design of the intake sections makes it possible to decelerate the flow to avoid cavitation in the rotating blades. Another advantage is that waterjets performance has little dependence on the advancing speed, making them the preferred solution for applications operating in shallow waters or when good manoeuvrability is required, e.g., in military amphibian vehicles (Park *et al.,* 2005). An optimal mass-flow-rate delivered at the pumping device is fundamental for the system to operate efficiently. This fact explains why the waterjet intake represents the most critical component to be designed since its functioning inevitably affects the performance of the other elements and the entire system (Huang *et al.,* 2019).

In these concerns, flush type systems are the most popular configuration, even though pod type installations can be found. In particular, the latter are characterised by higher losses due to the flow encounters' turning path before reaching the pump (Allison, 1993). As regards flush intakes, the power losses related to the sucked flow have been extensively studied by Bulten (2006), where the four conditions causing non-uniform distribution at the pump were identified as boundary layer ingestion, flow deceleration through the inclined diffusor, the presence of the shaft and the bending of the intake duct. Several studies were conducted to validate reliable numerical models to be used in prediction; thus, reducing the efficiency drops on the intake ducting (Park *et al.* 2005; Cao *et al.* 2017). The pump's conceptual design was efficiently addressed, and numerically validated by Oh *et al.* (2003). In recent times, the growing interest in bio-inspired optimisation in fluid machinery has made it possible to successfully enhance the performance of a mixed-flow pump through genetic algorithms (Huang *et al.,* 2015).

The present work aims at introducing to the marine environment a real innovation rather than an improvement of the existing technologies. The electrically driven ram inlet waterjet here discussed is an outboard device housing the whole propulsive system. This configuration overcomes the common propulsors' known limits by delivering a uniform mass flow rate to the pump. Besides, the rotor's rim driven arrangement makes it possible to discard the detrimental effects of the obstructing shaft. The present preliminary analysis focuses on the impact of the nacelle's shape on the system's overall resistance. A 2D axisymmetric domain is adopted for the solution of Reynolds-Averaged Navier Stokes (RANS) equations, coupled with $k-\omega$ Shear Stress Transport (SST) turbulence model. The

parametric study on the geometrical variants is carried out by varying the mass flow rate in a span of machine flow coefficient of 0.32, evenly subdivided into 8 intervals. As for the cruise velocities, far-field conditions are expressed as a range of highlight-diameter-based Reynolds number of $1.6 \cdot 10^6 \div 2.7 \cdot 10^6$, the latter based on propulsor's highlight diameter and free stream velocity. Axial length and outline curvature represent two crucial design drivers for the reduction of the drag coefficient. In particular, longer shapes provide smoother walls' profiles, promoting the decrease of the external hydrodynamic resistance despite the augmented wet surface.
The discussion is organised as follows: Section 2 outlines the geometrical variants and the details about the computational domain. The metrics of the analysis are here introduced as well. In Section 3 the results are presented and discussed, starting from the grid sensitivity study. Finally, Section 4 states the conclusions.

2 COMPUTATIONAL STRATEGY

2.1 Numerical model and solver setup

The results here discussed represent the first step of a thorough optimisation study for the external geometry of the propulsor (Fig. 1a). As a fully submerged device, the shape of its nacelle markedly affects either the performance of the jet and the resistance of the whole arrangement. Due to its derivation from the aeronautical environment, the investigation can take advantage of the extensive literature already published in the field of turbofans' shrouds optimisation (Magrini *et al.* 2020; Magrini *et al.* 2021; Ramirez-Rubio and MacManus 2020; Christie 2016). Accordingly, a proper exploration of the design space is necessary to restrict the set of possible designs, thus increasing the effectiveness during the pursuit of the optimum. The maximum cross section's impact and the curvature of the outline on the propulsor's drag are analysed. To this end, a baseline geometry, namely *v1*, is gradually modified: a first variant, *v2.1*, is created with a smaller maximum diameter (-11.6%) and longer afterbody (+10.8%); then, its length is reduced (-4.9% of *v2.1*'s axial extension), thus generating a second variant, *v2.2*, which adds an increased curvature to the outline of the afterbody (Fig. 1b). The exhaust spike dimension is adapted accordingly for the nozzle throat to fulfil the thrust requirement. On the contrary, the internal portion of the forebody is kept almost unvaried among the three geometries.

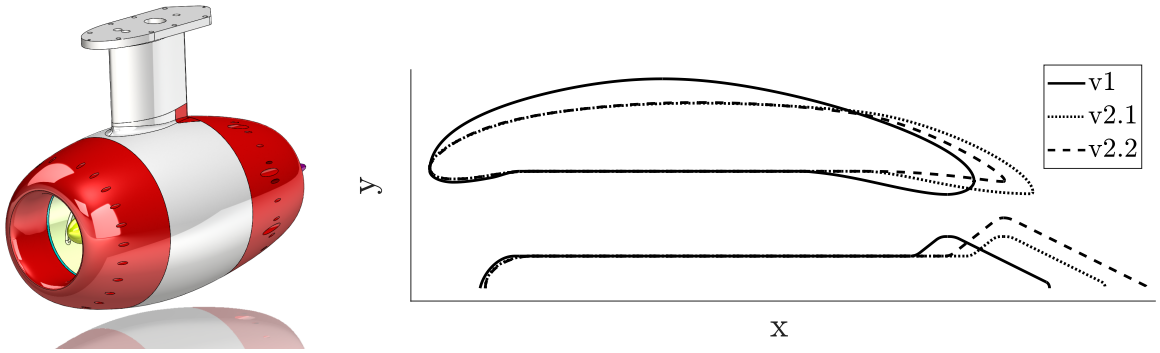

(a) **(b)**

Figure 1: Conceptual sketch of the full system (a) and 2D outlines of the three variants adopted for the axisymmetric computational model (b).

The fluid domain around the propulsor's walls is discretised with quadrilaterals, providing a 2D structured grid to be solved as an axisymmetric flow field about the system's axis of revolution. A multi-block strategy is adopted to assemble the whole mesh, from the wall-normal extruded layers to the far field boundary. The latter built as a semi-circle with the same center as the propulsor and a radius

of over 110 times the highlight diameter of the baseline geometry, D_{hl}. The wall distance of the first off-wall cell, y_1, is computed so as to provide a wall non-dimensional distance, $y_w^+ = \rho_w u_\tau y_1/\mu_w \leq 0.9$ where , ρ_w and μ_w being respectively fluid density and viscosity at the wall and u_τ denoting the friction velocity, estimated using the flat-plate boundary layer theory. In order for the grid to account for the higher velocities occurring at the nozzle, a 1D gas dynamics approach is adopted at the exhaust duct to estimate the throat maximum velocity to be used as reference value for evaluating the friction velocity. The nodes distribution is thickened in the neighbourhood of the corners of the geometry. The elements size from the walls to the far field is expanded following a root mean square principle, by adjusting the ends' values in order to guarantee a maximum equiangular skewness everywhere lower than 0.52, with low-quality cells located far from the walls' near-field.
A cut is created in the domain in the region corresponding to the pump housing. On the related vertical boundaries, a mass-flow-rate boundary condition is imposed. The far field boundary is equally split into two parts: the upstream half is set as velocity inlet, while pressure outlet is set on the other portion. An axis boundary condition is required to solve flow equations in a 2D axisymmetric shape. The free stream velocity, u_∞, is varied, yielding a Reynolds number $Re = \rho u_\infty D_{hl}/\mu$ in a range of $1.6 \cdot 10^6 \div 2.7 \cdot 10^6$. As regards the mass flow rate, $\dot{m}$, processed by the propulsor, for each cruise velocity 9 different values were considered. In particular, these were evenly distributed so as to provide an overall variation of the flow coefficient $\Delta\varphi = 0.32$, where $\varphi = \dot{m}/(\rho\Omega D_{ave}^3)$. Here D_{ave} is the average diameter of the pump section, while the angular velocity, Ω, as a preliminary design study, is kept constant for all the mass flow rates values.
The finite volume code ANSYS Fluent is adopted to solve the RANS equations over the computational domain. The 2-equation $k-\omega$ SST model is chosen as closure for the incompressible set of flow equations. A first set of iterations is run with a first-order discretisation method from a hybrid-initialised solution. Then, a third-order accuracy of the fluxes' approximation is adopted for reaching the convergence criterion, based on a value of $1 \cdot 10^{-5}$ for the root mean square of the residuals. A typical capture streamtube can be seen in Figure 2, through visualisation of the stream function's contour. The slight divergence of the streamlines near the highlight suggests a flow configuration that is consistent with a design operating condition meant for the propulsor.

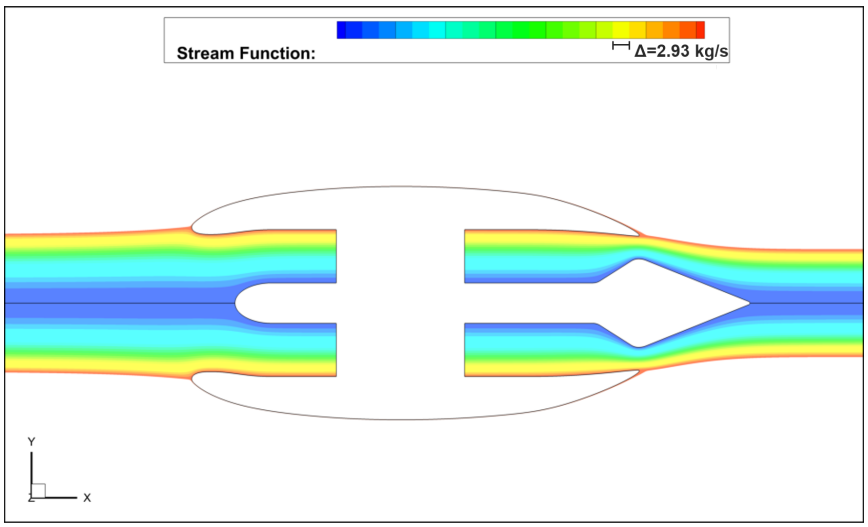

Figure 2: Capture stream tube through visualisation of stream function's contours for the third variant. The plot refers to a case with advancing speed of $Re = 1.6 \cdot 10^6$.

2.2 Performance parameters

The metrics adopted to evaluate the system's performance is the drag coefficient, c_d. Here, the drag of the nacelle accounts for the pre-entry effect, ϕ_{pre}, and the external cowl's wall resistance, ϕ_{nac}, as

follows (Stákowski *et al.,* 2016):

$$D_{nac} = \phi_{pre} + \phi_{nac} \tag{1}$$

Where the first term includes the variation of the flow momentum associated with the capture streamtube and is easily computed following Christie (2016), while the second term is calculated by integration of pressure and viscous stresses all over the outer surface of the shroud. The non-dimensional coefficient is recovered as $c_d = D_{nac}/(0.5\rho u_\infty^2 A_{hl})$, where $A_{hl} = \pi D_{hl}^2/4$. The Mass MFCR defines the operating conditions of the propulsor as an indicator of the location of the stagnation point along the cowl lip (Ramirez-Rubio and MacManus, 2020). Here, the computation slightly differs from that generally accepted in literature (Stákowski *et al.* 2016; Ramirez-Rubio and MacManus 2020; Magrini *et al.* 2021). In fact, the stagnation line is extracted, which defines the location of the stagnation point, r_{SP}, and the radius of the far-upstream cross-sectional area, r_∞. The MFCR is then given as the squared ratio between these two quantities.

3 RESULTS AND DISCUSSION

3.1 Grid sensitivity

As a novel system, experimental measurements still lack, making it impossible to thoroughly validate the numerical model. However, a grid convergence study is conducted to evaluate the dependence of the chosen discretisation results. To this end, three refinement levels of the mesh are generated by doubling the nodes on the walls boundaries, namely: coarse, medium and refined, respectively characterised by 518k, 1.2m and 3m elements. These values correspond to refinement ratios, based on the coarse grid, of 2.3 and 2.5, in order. Simulations for this analysis were conducted for the most critical operating conditions of free stream flow and mass flow rate to account for the situation involving the highest velocities. As metrics for the convergence study, integral and local variables are considered, c_d and y_w^+. In the first case, the value obtained with the coarse mesh is taken as a reference, and the relative difference with the other values is investigated (Fig. 3a). The curve trend suggests that no significant improvement is provided by refinement, the maximum variation being limited to 0.6%. However, by considering the dimensionless wall distance on the hub walls (Fig. 3b) it is possible to notice that in the exhaust region, i.e. where the highest velocities occur, the two refinement levels show a better behaviour in predicting the near-wall regions. Although the coarse grid shows everywhere values below the unity, the medium refined mesh was chosen for the investigation as it represents the best compromise between sensitivity and computational time.

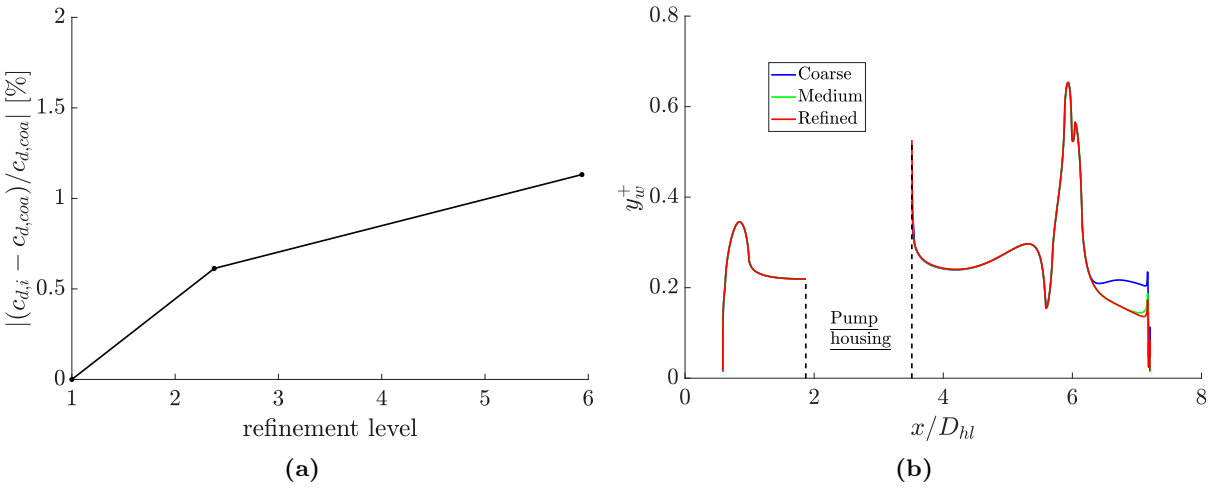

Figure 3: Relative variation of the nacelle drag coefficient as a function of the refinement level (a) and computed y_w^+ as a function of the non-dimensional axial coordinate along the hub walls (b).

3.2 Performance analysis

By imposing the mass flow rate on the pump housing boundaries, the pressure jump that the machine has to produce at the given design point is obtained from computations. The sudden increase of the flow enthalpy is visualised through total pressure (p_0) contours (Fig. 4a). Here, the external cowl impact on the system's viscous losses is clearly depicted, especially in the after-body region where the negative gradient of the walls induces boundary layer thickening. As a consequence, the design of this outline is fundamental to reduce hydrodynamic resistance. Similar considerations hold for the ending part of the spike. In fact, the thrust is a consequence of the change in the flow momentum between the propulsor's inlet and outlet. This is obtained thanks to the expansion nozzle, which converts the pressure content of flow discharged by the pump into kinetic energy (Fig. 4b) that feeds the momentum imbalance. Velocity contours emphasise the role of the spike's external wall in the overall drag accounting. These considerations suggest that the optimal solution concerning drag reduction lies in a geometry that reduces the cowl and spike gradients without affecting significantly the thrust generated by the throat section.

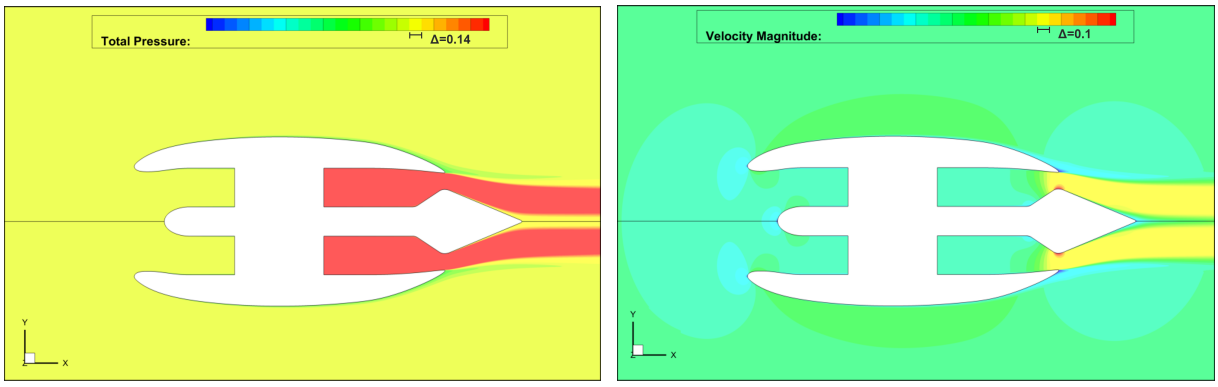

(a) **(b)**

Figure 4: Contours of non-dimensional total pressure, $p_0/p_{0,\infty}$, (a) and non-dimensional velocity magnitude, u/u_∞, (b) for the third variant, at $Re = 1.6 \cdot 10^6$.

In this regard, the analysis of the drag behaviour towards the geometrical variation allows for identifying the effectiveness of each modification. Figure 5a reports the curve of c_d as a function of the mass flow rate, here expressed as the machine flow coefficient, φ, for the flow condition at $Re = 1.6 \cdot 10^6$. The plot clearly shows that the second geometry generation, *v2*, reduces the propulsor's hydrodynamic resistance. This effect follows from the reduction of the maximum diameter, despite the substantial increase of wet surface due to the global length increment. This modification brings benefits in two ways: it decreases the overall cross-section area, which lowers the pressure (or form) drag, and it smoothens the gradients on the external walls, thus reducing the skin friction component associated with the viscous stresses. As far as the axial length, which sets the difference between *v2.1* and *v2.2*, it seems to act drastically on the performance. Although the global wet surface gets lowered, the additional curvature introduced at the external after-body is such that the c_d reaches values closer to the ones obtained for *v1*. One thing that is worth considering concerns the axial location of the nozzle throat. In this first analysis, this effect was not thoroughly investigated. However, it is planned for future studies to clarify how this parameter may also affect the distribution of the external flow.
Although the effect of the capture streamtube is included in the drag's computation, its shape does not seem to be effective on c_d, concerning the geometry. This can be stated by looking at Figure 5b, which reports the MFCR as a function of the same flow coefficients. Here, the curves for *v2.1* and *2.2* are almost overlapping, suggesting that the pre-entry streamtube has the same distribution. However, this fact does not prevent the marked discrepancy between the two drag curves. As for *v1*, the divergence of the MFCR from the other geometries should be attributed to the present flow regime: as the mass flow rate causes the stagnation point to move above the leading edge, the significant difference

among the geometries is responsible for the considerable separation among the plots. However, the variation (lower than 5%) is not such as to generate important effects on the curve in Figure 5a.

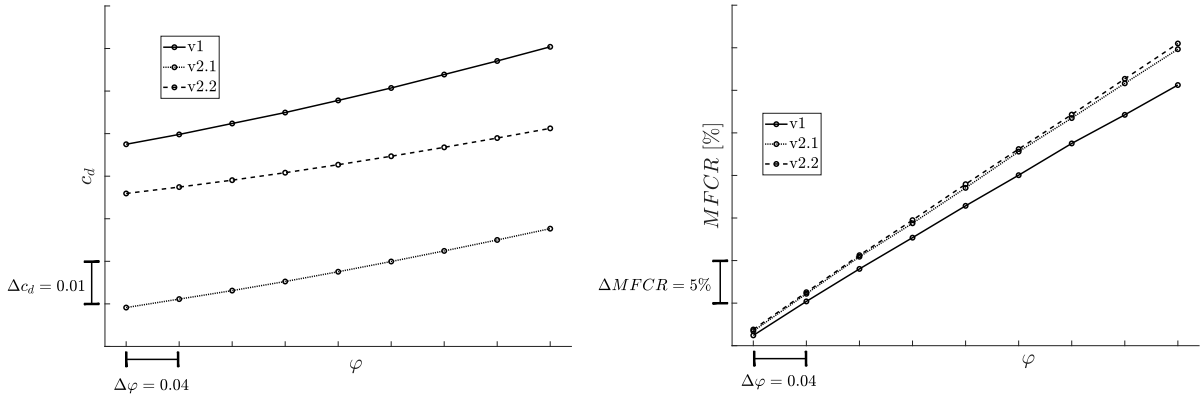

Figure 5: Drag coefficient (a) and mass flow capture ratio (b) as a function of the flow coefficient, comparing among the three variants. Simulations were carried with a flow velocity of $Re = 1.6 \cdot 10^6$.

The performance analysis at a higher free stream velocity ($Re = 2.7 \cdot 10^6$) follows the same considerations. This further investigation is intended to set the limiting operating conditions for the system. Expanding the study to a broad range of cruise speeds is important to give a complete insight into how the geometrical variations impact the performance even when the machine is not operating adequately. Here, the non-regularity of drag coefficient at the lower values of the flow coefficient (Fig. 6a) is due to the fact that the associated mass flow rates are incompatible with a feasible operating condition because of the extremely low values of MFCR and, thus, thrust. The monotonic trend is then recovered starting from the median value of φ. Regarding the variation of the drag coefficient, the second geometry maintains the same maximum separation as with the previous regime ($\Delta c_d \simeq 0.04$). On the contrary, the performance detriment brought by the further geometrical variation increases. In fact, in the previous case the maximum discrepancy with the baseline value was $\Delta c_d \simeq 0.02$, while in this case it is reduced to $\Delta c_d \simeq 0.009$, which suggests that at these operating conditions *v2.2* performs even more similarly to *v1*.

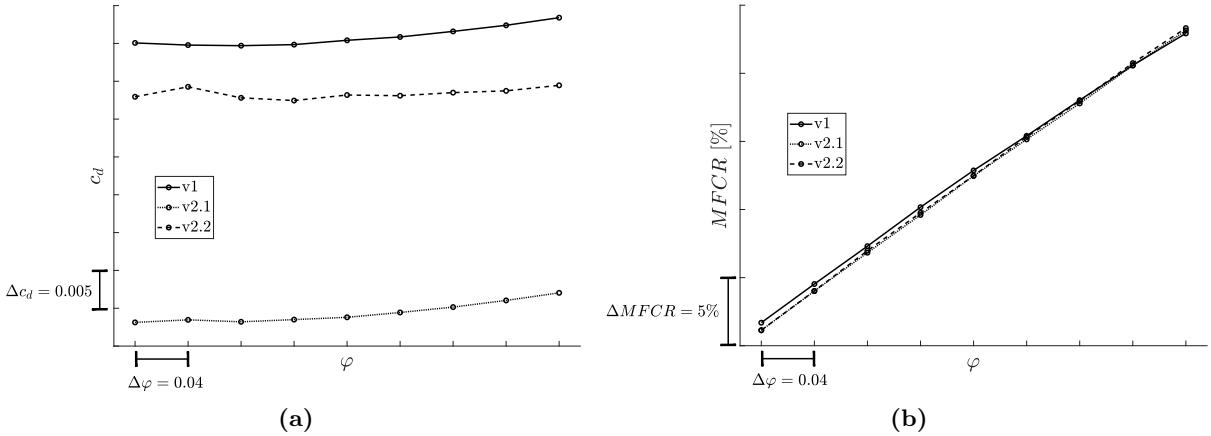

Figure 6: Drag coefficient (a) and mass flow capture ratio (b) as a function of the flow coefficient, comparing among the three variants. Simulations were carried with a flow velocity of $Re = 2.7 \cdot 10^6$.

The MFCR plot (Fig. 6b) further confirms the translation of the stagnation point below the highlight, as the cruise velocity gets higher. The curves are now almost overlaid, which denotes the similarity

of the shapes of the three pre-entry streamtubes. This behaviour relates to the fact that the internal outline is the same for the three variants. As a result, as the capture section narrows, the stagnation streamline is released from an unchanged location among the geometries. This fact is a shred of additional evidence that the ϕ_{pre} has a lower impact than the ϕ_{nac} on the overall resistance at the operating conditions here investigated, and it can be hardly considered as a primary driver for the enhancement of the system's performance.
The previous discussion corroborates the idea that this kind of waterjets should favour long flat geometries that minimise the negative gradients' magnitude on the walls. To this end, a key approach for the design of the nozzle throat restriction required for thrust generation lies in a proper trade-off solution that sizes together with the shape of the cowl after-body and the exhaust spike outline.

4 CONCLUSIONS

A design space exploration is conducted for a novel concept of waterjet propulsor. The innovation of the present unit is represented by the fact that a single outboard device houses the whole propulsion system, where the electrically rim driven pump allows for the suppression of the internal turbine and the associated losses due to the rotating shaft obstruction and intake shape turnings. As a fully submerged body, peculiar care is required in the nacelle design in that this component affects either the propulsive performance and overall hydrodynamic resistance. In this regard, this first study focuses on the impact of the propulsor's axial length and after-body curvature on the system's drag. To this end, a baseline geometry, namely *v1*, is further modified into two geometrical variants, respectively named *v2.1* and *v2.2*. Here, the definition of the coefficient follows the guidelines drawn by literature on aero-engines design, where the drag book-keeping suggests including the augmented resistance due to the shape of the pre-entry streamtube.
Here, the flow field is obtained through the numerical solution of the Reynolds-Averaged Navier-Stokes (RANS) system of equations over a 2D axisymmetric computational domain. Coupling with $k-\omega$ SST model allows for turbulence closure. Simulations are run by varying the mass flow rate imposed at the pump boundaries for 9 values, evenly distributed on a span of flow coefficient $\Delta\varphi = 0.32$. Free stream velocity is varied to provide Reynolds numbers in a range of $1.6 \cdot 10^6 \div 2.7 \cdot 10^6$; the latter based on the propulsor's highlight diameter. The comparison of the drag coefficient among the geometries shows that by decreasing the maximum diameter of the system, it is possible to reduce the overall hydrodynamic resistance as a consequence of two combined effects: a lowered cross-sectional area and a flattering outline that diminishes the boundary layer thickening caused by negative gradients. Despite decreasing the wet surface, a further shortening of the external cowl introduces an augmented curvature at the after-body that acts as a detriment to the system's performance. Simultaneous analysis of the pre-entry streamtube through the Mass Flow Capture Ratio (MFCR) makes it possible to conclude that the associated drag has a lower impact on the overall drag than the nacelle shape. In particular, this holds when the stagnation line detaches from a point located in the internal walls on the intake, which is typical for in-design operations. Consequently, this parameter can be hardly controlled to enhance the performance when a significant variation of the inner duct geometry is not expected.
Future investigations are meant to provide a thorough optimisation of the geometry. By defining a complete parameterisation of the whole outline, it will be possible to fully control the curves, thus making it possible to consider a broader range of factors. In this regard, genetic algorithms are a strategy that has already proved reliable in recovering efficient and optimised solutions in the field of aero-engines design due to its ability to deal with multi-objective multi-point investigations.

REFERENCES

[1] Allison, J. (1993). Marine Waterjet Propulsion. *SNAME Transactions*, **101**:275–335.

[2] Bulten, N. W. H. (2006). Numerical Analysis of a Waterjet Propulsion System. *PhD thesis*, Technische Unioversiteit Eindhoven.

[3] Cao, P., Wang, Y., Kang, C., Li, G., and Zhang, X. (2017). Investigation of the Role of Non-Uniform Suction Flow in the Performance of Water-Jet Pump. *Ocean Engineering*, **140**:258–269.

[4] Christie, R. (2016). Propulsion System Integration and Modelling Synthesis. *PhD thesis*, University of Cranfield.

[5] Huang, R., Dai, Y., Luo, X., Wang, Y., and Huang, C. (2019). Multi-Objective Optimization of the Flush-Type Intake Duct for a Waterjet Propulsion System. *Ocean Engineering*, **187**:106172.

[6] Huang, R., Luo, X., Ji, B., Wang, P., Yu, A., Zhai, Z., and Zhou, J. (2015). Multi-Objective Optimization of a Mixed-Flow Pump Impeller Using Modified Nsga-II Algorithm. *Science China Technological Sciences*, **12**:58.

[7] Magrini, A., Benini, E., Yao, H.-D., Postma, J. and Sheaf, C. (2020). A Review of Installation Effects of Ultra-High Bypass Ratio Engines. *Progress in Aerospace Sciences*, **119**:100680.

[8] Magrini, A., Buosi, D., Benini, E. and Sheaf, C. (2021). Ultra-High Bypass Nacelle Geometry Design Space Exploration. *AIAA Scitech 2021 Forum*, 1–13.

[9] Oh, H., Yoon, E., Kim, K. S., Ahn, J. (2003). A Practical Approach to the Hydraulic Design and Performance Analysis of a Mixed-Flow Pump for Marine Waterjet Propulsion. *Proceedings of the Institution of Mechanical Engineers, Part A: Journal of Power and Energy*, **217**:659–664.

[10] Park, W. G., Yun, H. S., Chun, H. H. and Kim, M. C. (2005). Numerical Flow Simulation of Flush Type Intake Duct of Waterjet. *Ocean Engineering*, **32**:2107–2120.

[11] Ramirez-Rubio, S. and MacManus, D.G. (2020). Framework for Estimation of Nacelle Drag on Isolated Aero-Engines with Separate Jets. *Proceedings of the Institution of Mechanical Engineers, Part G: Journal of Aerospace Engineering*, **234**:2025–2040.

[12] Stákowski, T.P., MacManus, D.G., Sheaf, C.T.J. and Christie, R. (2016). Aerodynamics of Aero-Engine Installation. *Proceedings of the Institution of Mechanical Engineers, Part G: Journal of Aerospace Engineering*, **230**:2673–2692.